

## SPATIAL FEATURES OF REYNOLDS-STRESS CARRYING STRUCTURES IN TURBULENT BOUNDARY LAYERS WITH PRESSURE GRADIENT

**Taygun Recep Gungor**

Department of Mechanical Engineering  
Universite Laval  
Quebec City, QC, G1V 0A6 Canada  
taygun-recep.gungor.1@ulaval.ca

**Mehmet Ali Yesildag**

Faculty of Aeronautics and Astronautics  
Istanbul Technical University  
34469, Istanbul, Turkey  
yesildag18@itu.edu.tr

**Ayse Gul Gungor**

Faculty of Aeronautics and Astronautics  
Istanbul Technical University  
34469, Istanbul, Turkey  
ayse.gungor@itu.edu.tr

**Yvan Maciel**

Department of Mechanical Engineering  
Universite Laval  
Quebec City, QC, G1V 0A6 Canada  
yvan.maciel@gmc.ulaval.ca

### ABSTRACT

Two direct numerical simulation databases are examined to understand the effect of mean shear on the outer layer turbulence of pressure-gradient turbulent boundary layers along with two homogeneous shear turbulence databases. We compare the shape of Reynolds-shear-stress carrying structures in all cases, choosing five streamwise locations in the turbulent boundary layers with different pressure gradient sign and/or intensity, as well as upstream history. The results indicate that the shape of the structures is very similar across all flows when their size is between 1 to 10 Corrsin length scales. This suggests that mean shear acts in a similar manner in all these flows to generate Reynolds-shear-stress carrying structures and therefore turbulence production.

### INTRODUCTION

When a turbulent boundary layer (TBL) is exposed to an adverse pressure gradient (APG), the mean velocity defect becomes significant, resulting in higher mean shear in the outer layer and reduced shear near the wall. These changes lead to significant alterations in turbulence characteristics. In canonical wall-bounded flows like channel flows or zero-pressure-gradient (ZPG) TBLs, turbulence is dominant in the inner region. Unlike canonical flows, in APG TBLs with large velocity defect, Reynolds stresses reach their highest values in the outer layer (Maciel *et al.*, 2018). Moreover, turbulence production in the outer layer of APG TBLs surpasses that in the inner layer (Gungor *et al.*, 2022). Even in APG TBLs with a small velocity defect, where the Reynolds stresses do not exhibit an outer peak, Reynolds stress levels are elevated in the outer layer. The increased turbulence activity in the outer layer is a crucial distinction between APG TBLs and canonical wall flows, underscoring the significance of the outer layer in APG TBLs.

Gungor *et al.* (2016) and Kitsios *et al.* (2017) suggested that large-defect APG TBLs resemble free-shear flows due to the changes in the mean velocity profiles. Besides APG TBLs, Dong *et al.* (2017) demonstrated that large-scale sweeps and ejections in the overlap layer of channel flows, which carry

most of the Reynolds shear stress, resemble those found in homogeneous shear turbulence (HST). They concluded that these large-scale structures are associated with the local mean shear, rather than with the presence of a wall. Later, Gungor *et al.* (2020) examined sweeps and ejections in the outer layer of an APG TBL and also observed that they resemble those in HST. Furthermore, their findings indicated that outer layer turbulence in APG TBLs with a significant velocity defect is only minimally influenced by turbulence in the near-wall region.

In this work, we extend the study of Gungor *et al.* (2020) by considering a wider variety of pressure gradient situations and flow histories of non-equilibrium TBLs. We examine the spatial characteristics of Reynolds-shear-stress carrying structures through their aspect ratios for two direct numerical simulation (DNS) databases. These flow cases are the non-equilibrium PG TBLs of Gungor *et al.* (2022) with a  $Re_\theta$  reaching 8650 and of Gungor *et al.* (2024) with a  $Re_\theta$  reaching 13000.

### FLOW DESCRIPTION

Figure 1a shows the spatial evolution of the pressure gradient parameter based on Zagarola-Smits velocity ( $U_{ZS}$ ),  $\beta_{ZS} = (\delta/\rho U_{ZS}^2)(dp_e/dx)$ , for the two PG TBLs, where  $\delta$  is the local boundary layer thickness and  $p_e$  is the pressure at the edge of the BL.  $\beta_{ZS}$  follows the ratio of pressure force to the turbulent force in the outer layer (Maciel *et al.*, 2018). DNS23 evolves from a ZPG TBL to a TBL with a large velocity defect first but then later it is exposed to a favourable pressure gradient (FPG), which results in a FPG TBL with a flow history of an APG TBL. DNS22 is a non-equilibrium APG TBL, which evolves from a ZPG TBL to a TBL on the verge of separation. The shape factor distribution in figure 1b shows the difference between the two cases. DNS22 is in stronger disequilibrium than DNS23, whereas the Reynolds number is higher in DNS23 than in DNS22.

For analyzing the flows in detail, we choose two streamwise positions from DNS22 and three positions from DNS23 and collect spatio-temporal data from these positions. The first position of each flow has a small velocity defect ( $H = 1.65$  and

Table 1: The main properties of the flow cases.

Position	$H$	$Re_\theta$	$Re_\tau$
ZPG	1.35	6500	1989
DNS22-APG1	1.65	2985	626
DNS23-APG1	1.60	5259	1007
DNS23-FPG	1.60	12207	2182
DNS22-APG2	2.63	5769	455
DNS23-APG2	2.78	10306	696

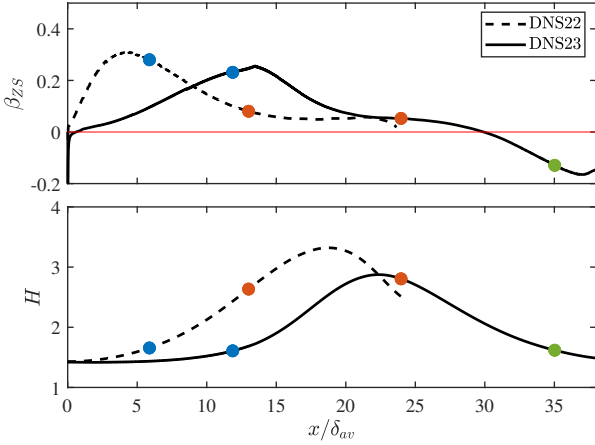


Figure 1: The  $\beta_{zs}$  and  $H$  distribution of the TBL cases.

1.60 for DNS22 and DNS23, respectively) while the second one has a large velocity defect ( $H=2.63$  and  $2.78$ , for DNS22 and DNS23, respectively). The third position of DNS23 has the defect of the first position ( $H = 1.60$ ) but the flow is under the effect of a FPG and a long non-equilibrium history. The ZPG TBL of Sillero *et al.* (2013) at  $Re_\tau = 1306$  is also used as a reference case. Table 1 summarizes the main parameters of these streamwise positions.

Figure 2 presents the mean velocity and the  $\langle u^2 \rangle$  profiles as a function of  $y/\delta$  for the cases described above. In both the small- and large-defect APG cases, the two flows exhibit similar mean velocity profiles at comparable  $H$  values. However, differences arise due to small variations in  $H$  values, distinct flow histories, and Reynolds numbers. The FPG case exhibits a distinct mean velocity profile compared to the small-defect APG TBL cases, attributed to its APG-FPG flow history. However, the mean shear is similar above  $y/\delta = 0.3$ . Figure 2b illustrates, as widely reported in the literature, that outer layer turbulence becomes dominant as the defect increases. In the small-defect APG cases (blue lines), the higher levels of  $\langle u^2 \rangle$  observed in DNS22 align with the larger  $H$  and mean shear, while the contribution of flow history remains relatively small. Conversely, in the large-defect APG cases (orange lines), the larger mean shear and more gradual increase of the APG result in higher levels of  $\langle u^2 \rangle$  for DNS23. Regarding the  $\langle u^2 \rangle$  profile of the FPG case, although it has recovered the near-wall peak, its outer level is much higher than those of the small-defect APG TBLs and resembles those of the large-defect cases. This indicates a delayed response of outer turbulence. Thus, we

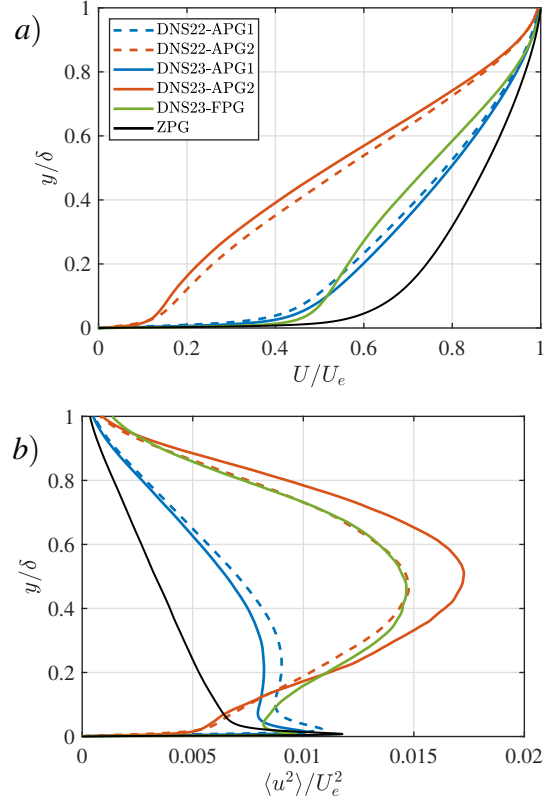


Figure 2: The mean velocity (top) and  $\langle u^2 \rangle$  profiles of the selected flow cases as a function of  $y/\delta$ .

have a set of flow cases that combine both similar and very different PG TBLs.

To understand the importance of the mean shear for the outer layer, we examine the Corrsin shear parameter ( $S^*$ ) in all cases.  $S^*$  is defined as  $S^* = Sq^2/\varepsilon$ , where  $S$  is the mean shear,  $q^2$  is twice the turbulence kinetic energy and  $\varepsilon$  is turbulence dissipation. It indicates the importance of the interaction between the shear and energy-carrying structures. When  $S^*$  is much greater than 1, these structures are primarily influenced by the local mean shear. Conversely, when  $S^*$  is less than or approximately equal to 1, turbulence becomes disconnected from the mean shear (Jiménez, 2013). Figure 3a presents  $S^*$  as a function of  $y/\delta$  for the TBL cases.  $S^*$  remains fairly constant between  $y/\delta = 0.3$  and  $0.8$  for all cases except DNS23-FPG where it is constant between  $y/\delta = 0.4$  and  $0.8$ .

We employ the Corrsin length scale ( $L_c$ ) as the length scale for the structures to evaluate the effect of mean shear on these structures.  $L_c$  is defined as  $(\varepsilon/S^3)^{1/2}$ . The Corrsin length scale is an intermediate length scale that represents the size of the smallest structures interacting with the mean shear. When  $L_c < 1$ , turbulent structures are decoupled from mean shear and become isotropic in size. Figure 3b shows the Corrsin length scale ( $L_c$ ), normalized with  $\delta$ , and plotted as a function of  $y/\delta$ . One striking result is that the behaviour of  $L_c/\delta$  profiles are very similar for each defect situation (ZPG/APG1 (small velocity-defect), APG2, and FPG) in the region between  $y/\delta = 0.3$  and  $0.8$ .

In addition to these databases, we employ two HST databases with Taylor microscale Reynolds numbers of 104 and 248, as described in detail by Dong *et al.* (2017), to better understand the influence of mean shear in the outer layer.

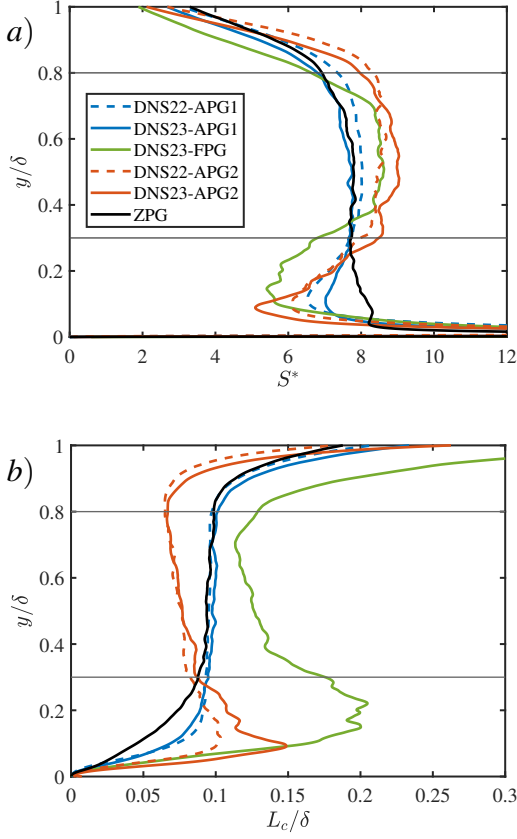


Figure 3: The Corrsin shear parameter (a) and Corrsin length scale (b) for the TBL cases as a function of  $y/\delta$ .

## RESULTS

### Structure Identification Method

We examine the Reynolds-shear-stress carrying structures and they are classified into four groups based on their quadrant position in the  $u$ - $v$  plane: outward interactions ( $Q1$ ,  $u > 0$  and  $v > 0$ ), ejections ( $Q2$ ,  $u < 0$  and  $v > 0$ ), inward interactions ( $Q3$ ,  $u < 0$  and  $v < 0$ ) and sweeps ( $Q4$ ,  $u > 0$  and  $v < 0$ ). For this work, we only consider the intense  $Q2$ s and  $Q4$ s, which are the ones that predominantly carry the Reynolds shear stress. To identify these intense  $Q2$  and  $Q4$  structures, we employ the clustering technique where structures are defined as connected regions satisfying the following condition (Lozano-Durán *et al.*, 2012; Maciel *et al.*, 2017b):

$$|u(\mathbf{x})v(\mathbf{x})| > H^* \sigma_u \sigma_v. \quad (1)$$

Here,  $H^*$  is the threshold constant and  $\sigma$  is the root-mean-square of the velocity fluctuation denoted by the index. Connectivity is defined with the six orthogonal neighbours in the mesh of the DNS. The value of  $H^*$  was determined to be 1.75 through percolation analysis by Lozano-Durán *et al.* (2012) for channel flows and by Maciel *et al.* (2017b) for various APG TBLs. Because of its consistent value, we adopt  $H^* = 1.75$  without conducting further percolation analysis.

For this study, the  $Q$  structures are identified using spatio-temporal data, with the streamwise direction being temporal and the wall-normal and spanwise directions being spatial. Taylor's frozen turbulence hypothesis is applied to each  $Q$

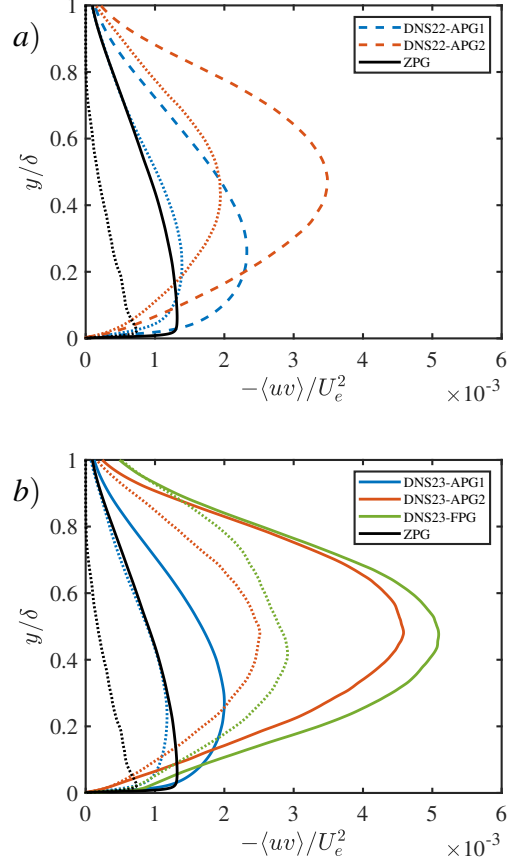


Figure 4: Reynolds shear stress profiles (solid lines) compared with the Reynolds shear stress carried by the identified intense  $Q^-$  events (dotted lines) for DNS22 (a) and DNS23 (b).

structure individually to convert time into the streamwise direction  $x$ , utilizing the local mean velocity at the structure's center as the convection velocity. The  $y$  location of the structure's centre is calculated by taking the arithmetic mean of its minimum and maximum  $y$  locations.

Figure 4 compares the amount of Reynolds shear stress carried by the identified  $Q^-$  structures, where  $Q^-$  stands for combined intense  $Q2$ s and  $Q4$ s, to the total Reynolds shear stress as a function of  $y/\delta$  for all cases along with the ZPG TBL of Sillero *et al.* (2013). With the chosen extraction threshold value ( $H^* = 1.75$ ), the identified  $Q^-$  structures carry approximately half of the total amount of Reynolds shear stress in all cases.

We distinguish between wall-attached and wall-detached  $Q$  structures due to their known differences in properties and dynamic significance. In canonical wall flows, wall-attached  $Q$  structures are larger and predominantly carry the Reynolds shear stress in the overlap layer (Lozano-Durán *et al.*, 2012; Maciel *et al.*, 2017a,b). However, in large-defect APG TBLs, detached  $Q$  structures become more numerous and contribute equally to the Reynolds shear stress as attached ones (Maciel *et al.*, 2017a). Attached structures are defined as those with a minimum distance to the wall less than  $0.05\delta$ , while the rest are considered detached structures. The joint probability density functions of the minimum and maximum wall distances of the  $Q$ s (not shown) confirm that this boundary at  $y = 0.05\delta$  adequately separates both types of structures.

Table 2: Parameters of the attached/detached structures.  $N_i$  and  $V_i$  are the percentages of  $Q$  of each class in terms of their number and volume.

Position	NQ2		NQ4		VQ2		VQ4	
	Attached	Detached	Attached	Detached	Attached	Detached	Attached	Detached
DNS22-APG1	16.9	31.5	18.4	33.2	34.9	25.2	13.3	26.7
DNS22-APG2	2.9	42.2	4.5	50.4	31.2	29.6	15.9	23.3
DNS23-APG1	18.2	31.2	19.1	31.6	42.6	20.5	15.7	21.3
DNS23-APG2	2.0	42.6	3.4	52.0	26.7	31.2	19.9	22.3
DNS23-FPG	13.2	35.0	14.3	37.5	51.3	11.7	23.5	13.6

Table 2 shows the percentage of the attached and detached  $Q^-$ s in terms of their number and volume for the present flow cases. In all flow cases, there are far more detached structures than attached ones. Despite this, the volume occupied by attached and detached structures tends to be similar overall, with two exceptions. Firstly, in the small-defect APG TBLs, attached Q2s occupy more volume than detached ones, as in canonical wall flows. Secondly, in the FPG TBL, both types of attached Qs occupy significantly more space than their detached counterparts.

## Reynolds Shear Stress Contributions

After identifying the  $Q$  structures, we investigate the contribution of each type of  $Q$  to the Reynolds shear stress. Figure 6 illustrates the Reynolds shear stress contributions from intense  $Q$  structures separated both in quadrant type and attached/detached type, as a function of  $y/\delta$  for DNS23 and the ZPG TBL case of Sillero *et al.* (2013). It is important to stress that the contributions are normalized with the local  $\langle uv \rangle$  and therefore it may give the impression that the Reynolds shear stress increases towards the boundary layer edge, which is not the case as shown in figure 4. The behavior of intense Qs exhibit similarities in all cases. The contribution to the Reynolds shear stress predominantly comes from the  $Q^-$  structures (Q2s and Q4s). Moreover, the contribution of Q2s and Q4s increases and decreases with  $y$ , respectively.

Despite these similarities, the pressure gradient alters the structures significantly. In the lower part of the boundary layer, the contribution of  $Q^+$ s (Q1s and Q3s) become more relevant for the large-defect case APG2. Their intensity is at the same levels as Q2s in APG2 whereas it is small in APG1. Moreover, the Q4 structures are the most important structures in the lower half of APG2. This is not the case for ZPG and APG1 where Q2s' and Q4s' contributions are at the same level except the very near-wall region where Q4s' contribution peaks in all cases. The differences show the effect of the velocity defect and consequently the pressure gradient on structures.

In the FPG case, the contribution of Q2s and Q4s are comparable in the lower half of the boundary layer. Furthermore, the  $Q^+$ s' importance decreases but they are still higher than for APG1 and ZPG. One important difference of the FPG and the other three cases is that the attached structures dominate the flow even in the upper part of the boundary layer. This could be due, at least in part, to the downward (negative  $v$ ) advection of the structures in the FPG region.

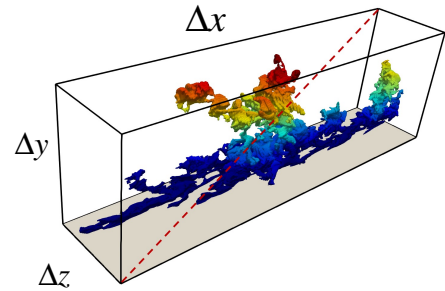


Figure 5: A  $Q2$  structure with the circumscribing box used to indicate the size of the structure. The dashed line shows the diagonal.

## Size and shape of the structures

In this study, as discussed above, we examine the spatial features of Q2s and Q4s in the region between  $y/\delta = 0.3$  and  $0.8$ . Therefore, structures whose centres are outside of this region are discarded from the analysis. Besides this, we only consider wall-detached structures for this analysis, because wall-attached structures can be geometrically affected by the wall and their spatial features can be very different from those of wall-detached ones (Dong *et al.*, 2017). By doing that, we aim to isolate the effect of the mean shear in different flow cases. Table 3 presents the number and volume of detached Q2 and Q4 structures in the region between  $y/\delta = 0.3$  and  $0.8$ . The number of Q2s is slightly less than Q4s in all flow cases. For their volumes, which are more important than their numbers, Q2 structures occupy a larger volume than Q4s in the APG TBL cases. The ratio of the volume Q2s occupy to the volume Q4s occupy is very similar in all APG cases. Contrary to this, Q4s have a larger volume in the FPG case. Nonetheless, it can be said that both Q2s and Q4s are relevant in the region of interest of all flow cases.

To investigate the spatial features of the  $Q$  structures, we utilize their aspect ratios because they provide information of the shape of Qs and whether they are isotropic or not. Figure 5 shows a single Q2 structure with the circumscribing box extracted from D23-APG1. The dimensions of the box are utilized as the dimensions of the structure. Figure 7 shows the average aspect ratio ( $a_{ij} = \Delta_i/\Delta_j$ ) for all cases as a function of the diagonal of the structures ( $d = \sqrt{\Delta_x^2 + \Delta_y^2 + \Delta_z^2}$ ). The box diagonal  $d$  is normalised with  $L_c$ . In addition to this, we employ two HST cases of Dong *et al.* (2017) for comparison. We utilize these two HST cases, which are the same case with different Reynolds numbers, to see the effect of a flow driven

Table 3: Parameters of the structures used in the paper. Structures are between  $0.3\delta < y_c < 0.8\delta$  and  $y_{min} > 0.05\delta$ .  $N_i$  and  $V_i$  are the percentages of Qs of each class in terms of their number and volume.

Position	$N_2$	$N_4$	$V_2$	$V_4$
DNS22-APG1	46.4	53.7	62.8	37.2
DNS23-APG1	47.7	52.3	59.3	40.7
DNS22-APG2	44.1	56.0	61.5	38.5
DNS23-APG2	44.3	55.7	62.3	37.7
DNS23-FPG	49.2	50.8	45.5	54.5

by only shear, in the absence of a wall.

Figure 7(a, b) depicts the average aspect ratio  $a_{zy}$  and  $a_{xy}$  for all detached  $Q^-$ s between  $y/\delta = 0.3$  and  $0.8$  for the TBL cases along with the HST cases. The  $a_{zy}$  curves collapse almost perfectly for structures whose diagonals are between  $1L_c$  and  $10L_c$ . The aspect ratio is slightly above 1 and then decreases to slightly below 1 with increasing structure size until above approximately  $d = 10L_c$ . The diverging trends between HSTs and TBLs for large-scale structures above  $d = 10L_c$  are attributed to the distinct boundaries of these two types of flows. In HSTs, the ratio  $a_{zy}$  decreases due to the unbounded nature of structures in the  $y$  direction (Dong *et al.*, 2017). Conversely, in TBLs,  $a_{zy}$  increases as the structures are bounded in  $y$ .

The trend for  $a_{xy}$  is also very similar for all TBL cases between  $1L_c$  and  $10L_c$ . Furthermore, the TBL and HST cases coincide well for structures whose diagonal is between approximately  $d/L_c = 3$  and  $10$ . Overall, the similarity is less pronounced for  $a_{xy}$  compared to  $a_{zy}$ . This difference may happen for several reasons. The TBLs are in non-equilibrium in the streamwise direction, which is not the case for the HSTs. Moreover, we use Taylor’s hypothesis to estimate the streamwise length of structures. It is possible that the hypothesis fails for small-scale structures with a diagonal of  $d/L_c \approx 1 - 2$ . But more work is required to understand this difference.

Figure 7(c – e) illustrates separately the average aspect ratios for Q2s and Q4s. The trend for  $a_{zy}$  is almost identical for both Q2s and Q4s. This is important as it suggests Q2s and Q4s have similar spatial features in the spanwise direction with respect to their wall-normal height. The only deviation is for FPG case for Q4s above  $d/L_c \approx 7$ , where  $a_{zy}$  is slightly more than the others. As for  $a_{xy}$ , the trend is almost the same for all TBLs but the aspect ratio is different for Q2s and Q4s. The Q2 structures are streamwise elongated as their aspect ratio is around 1.5 while Q4 structures’ aspect ratio is slightly above 1.

The findings above show that the Q structures in the TBL cases and HSTs behave very similarly and almost identically in some cases when their diagonal is scaled with  $L_c$ . This perfectly highlights the major role the mean shear plays for Q structures and therefore for turbulence production.

## CONCLUDING REMARKS

In this study, we analyze the Q structures and the effect of mean shear on these structures in two non-equilibrium TBLs of Gungor *et al.* (2022) and Gungor *et al.* (2024) along with the HST cases of Dong *et al.* (2017). We identify individual Q structures in the flow and examine the spatial properties of de-

tached sweeps and ejections through their aspect ratios,  $a_{zy}$  and  $a_{xy}$ . For the TBLs, the region considered is the middle of the outer layer between  $0.3\delta$  and  $0.8\delta$ . The spatial characteristics of these structures seem to be governed by the mean shear as their aspect ratio behaves very similarly in all the flows, and all regions of the TBLs, when the size of the structures is normalized with the Corrsin length scale. The relative contribution of detached sweeps and ejections to the Reynolds shear stress, however, depends on the pressure gradient context in boundary layers.

## ACKNOWLEDGMENTS

We acknowledge PRACE for awarding us access to Marconi100 at CINECA, Italy and Calcul Québec (www.calculquebec.ca) and the Digital Research Alliance of Canada (alliancecan.ca) for awarding us access to Niagara HPC server. TRG and YM acknowledge the support of the Natural Sciences and Engineering Research Council of Canada (NSERC), project number RGPIN-2019-04194. TRG and AGG were supported by the research funds of Istanbul Technical University (project numbers:MDK-2018-41689)

## REFERENCES

- Dong, S., Lozano-Duran, A., Sekimoto, A. & Jiménez, J. 2017 Coherent structures in statistically stationary homogeneous shear turbulence. *Journal of Fluid Mechanics* **816**, 167–208.
- Gungor, A.G., Maciel, Y., Simens, M. & Soria, J. 2016 Scaling and statistics of large-defect adverse pressure gradient turbulent boundary layers. *International Journal of Heat and Fluid Flow* **59**, 109–124.
- Gungor, T.R., Gungor, A.G. & Maciel, Y. 2024 Turbulent boundary layer response to uniform changes of the pressure force contribution. *arXiv preprint arXiv:2402.13067*.
- Gungor, T.R., Maciel, Y. & Gungor, A.G. 2020 Reynolds shear-stress carrying structures in shear-dominated flows. *Journal of Physics: Conference Series* **1522**, 012009.
- Gungor, T.R., Maciel, Y. & Gungor, A.G. 2022 Energy transfer mechanisms in adverse pressure gradient turbulent boundary layers: production and inter-component redistribution. *Journal of Fluid Mechanics* **948**, A5.
- Jiménez, J. 2013 Near-wall turbulence. *Physics of Fluids* **25** (10), 101302.
- Kitsios, V., Sekimoto, A., Atkinson, C., Sillero, J.A., Borrell, G., Gungor, A.G., Jiménez, J. & Soria, J. 2017 Direct numerical simulation of a self-similar adverse pressure gradient turbulent boundary layer at the verge of separation. *Journal of Fluid Mechanics* **829**, 392–419.
- Lozano-Durán, A., Flores, O. & Jiménez, J. 2012 The three-dimensional structure of momentum transfer in turbulent channels. *Journal of Fluid Mechanics* **694**, 100–130.
- Maciel, Y., Gungor, A.G. & Simens, M. 2017a Structural differences between small and large momentum-defect turbulent boundary layers. *International Journal of Heat and Fluid Flow* **67**, 95–110.
- Maciel, Y., Simens, M. & Gungor, A.G. 2017b Coherent structures in a non-equilibrium large-velocity-defect turbulent boundary layer. *Flow, Turbulence and Combustion* **98**.
- Maciel, Y., Wei, T., Gungor, A.G. & Simens, M.P. 2018 Outer scales and parameters of adverse-pressure-gradient turbulent boundary layers. *Journal of Fluid Mechanics* **844**, 5–35.
- Sillero, J.A., Jiménez, J. & Moser, R.D. 2013 One-point statistics for turbulent wall-bounded flows at Reynolds numbers up to  $\delta^+ \approx 2000$ . *Physics of Fluids* **25** (10), 105102.

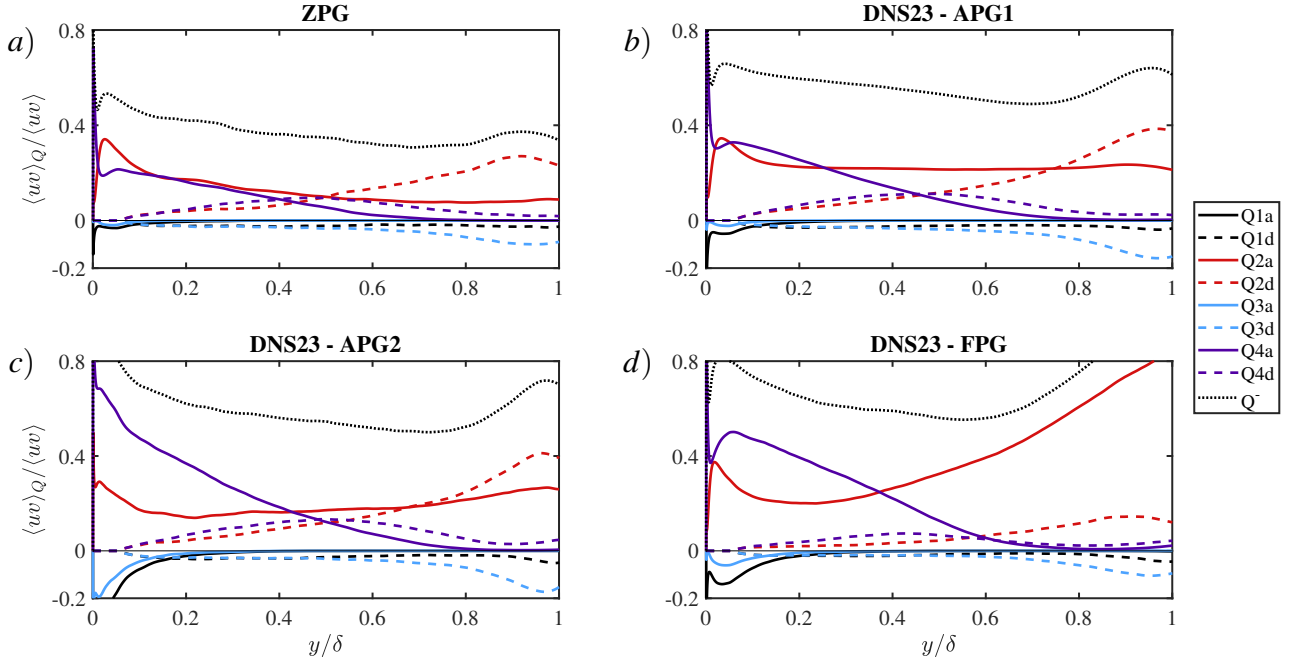


Figure 6: Fractional contributions to  $\langle uv \rangle$  from attached Qs (solid), and detached Qs (dashed) for ZPG (a), APG1 (b), APG2 (c), and FPG (d) of DNS23. The dotted line is the total fractional contribution of all Q2s and Q4s.

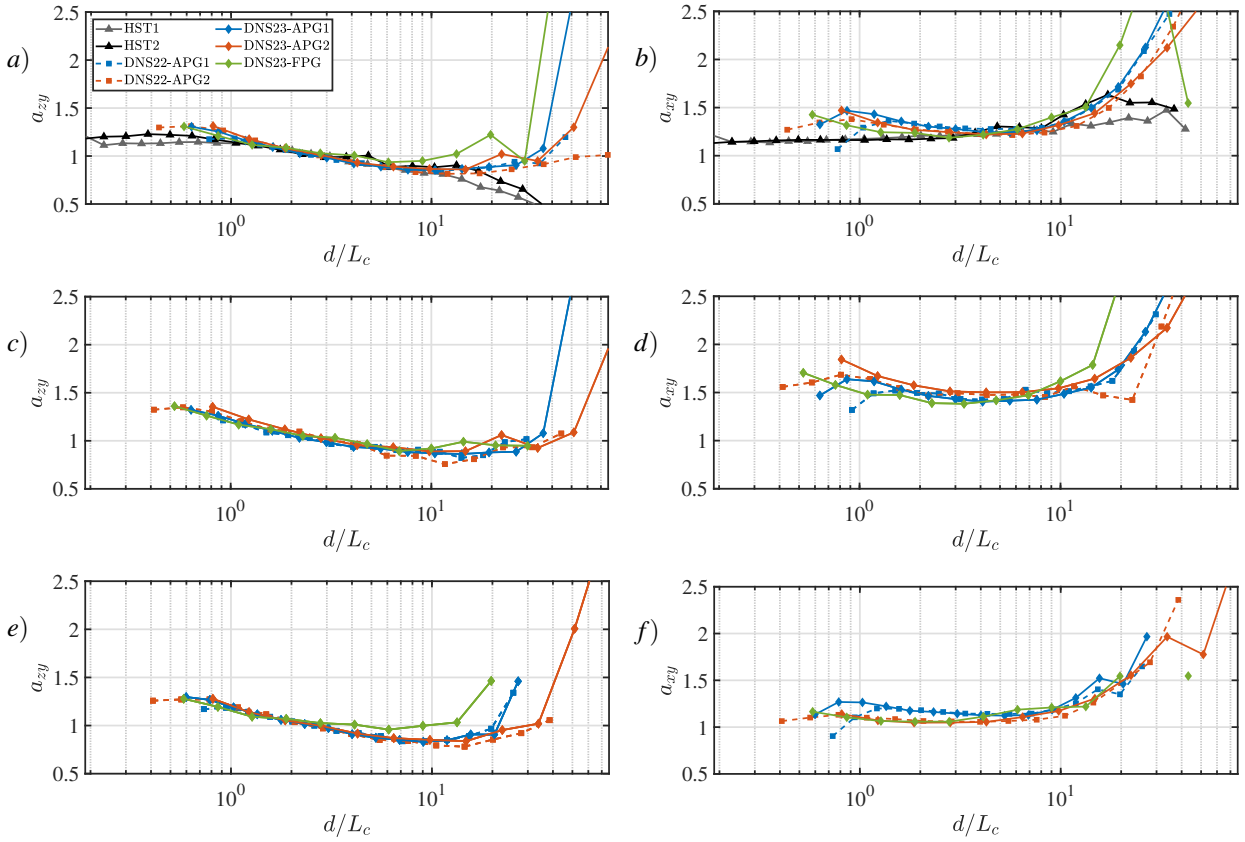


Figure 7: Average aspect ratio of the circumscribing boxes for detached  $Q^-$  structures whose center is between  $y/\delta = 0.3$  and 0.8 as a function of the box diagonal of the structure for all  $Q^-$ s combined (a,b), Q2s (c,d) and Q4s (e,f). The box diagonal is normalized with  $L_c$ .